Journal of Alloys and Compounds 1013 (2025) 178546

Contents lists available at ScienceDirect

Journal of Alloys and Compounds

journal homepage: www.elsevier.com/locate/jalcom

Zirconium aluminum nitride thin films for temperature sensing applications

Bruno Martins [a,b,*], Carlos Patacas [a,b], Albano Cavaleiro [a,b], Pedro Faia [c], Cristiana F. Almeida Alves [e], Enrique Carbo-Argibay [e], Paulo J. Ferreira [e,f,g], Filipe Fernandes [b,d]

[a] IPN - LED&MAT - Instituto Pedro Nunes, Laboratório de Ensaios, Desgaste e Materiais, Rua Pedro Nunes, Coimbra 3030-199, Portugal
[b] University of Coimbra, CEMMPRE, ARISE, Department of Mechanical Engineering, Rua Luís Reis Santos, Coimbra 3030-788, Portugal
[c] University of Coimbra, CEMMPRE – Electrical and Computer Engineering Department, FCTUC, Polo 2, Pinhal de Marrocos, Coimbra 3030-290, Portugal
[d] CIDEM, ISEP - School of Engineering, Polytechnic of Porto, Rua Dr. António Bernardino de Almeida 431, Porto 4200-072, Portugal
[e] International Iberian Nanotechnology Laboratory (INL), Avenida Mestre José Veiga s/n, Braga 4715-330, Portugal
[f] Mechanical Engineering Department and IDMEC, Instituto Superior Técnico, Av. Rovisco Pais 1, Lisboa 1049-001, Portugal
[g] Materials Science and Engineering Program, University of Texas at Austin, Austin, TX 78712, USA

ARTICLE INFO

Keywords:
NTC thin-film thermistor
Magnetron sputtering
$Zr_{1-x}Al_xN$ thin films
Multilayer coating
Temperature sensing
Industry 4.0

ABSTRACT

This study explores the development and characterization of zirconium aluminum nitride (ZrAlN) thin films produced via magnetron sputtering for temperature sensing applications. The sensor film is integrated into a fully nitride multilayer coating and designed to work in harsh environments. The ZrAlN demonstrated stable semiconductor behavior up to 750 °C, making it suitable for high-temperature thermistors, with a β value of approximately 850 K after signal stabilization. Detailed structural characterization confirmed a mixed-phase structure of poorly crystalline cubic ZrN and orthorhombic Zr_3N_4. This structure is believed to be responsible for the high resistivity of 8.0×10^5 μΩ·cm observed in $Zr_{1-x}Al_xN$ with $x = 0.3$. The examination of $Zr_{0.7}Al_{0.3}N$ integrated into the multilayer coating revealed a columnar morphology with diffuse nanolayers, alternating between aluminum-rich and aluminum-poor zones, caused by the two-fold rotational deposition. The sensor coating was further tested on a cutting tool substrate, with the $Zr_{0.7}Al_{0.3}N$ layer exhibiting a sensitivity of 800 K and demonstrating effective temperature measurements up to 400 °C. The $Zr_{0.7}Al_{0.3}N$ layer inserted in a nitride-based multilayer coating, combined with Arduino® for signal acquisition, resulted in a measured error of approximately 7 %. The setup presented the potential for integration into manufacturing environments aligned with Industry 4.0.

1. Introduction

Decades of research on transition metal nitrides (TMNs), such as titanium aluminum nitride (TiAlN) and zirconium aluminum nitride (ZrAlN), have established their superior thermomechanical properties [1,2]. These materials are recognized for their exceptional hardness and thermal stability, making them ideal for various demanding industrial applications [3,4]. Despite these well-documented mechanical and thermal characteristics, their semiconductor or thermoresistive properties, specifically their resistivity response to temperature changes, remain poorly understood. A comprehensive exploration of these properties could unlock new functionalities for TMNs, enabling surface protection and precise thermal monitoring.

Among largely used semiconductor sensors, thermistors with a negative temperature coefficient of resistance (NTCR), which exhibit a nonlinear decrease in resistance with increasing temperature, are of great interest. These sensors are mainly composed of transition metal oxides with spinel or perovskite structures [5]. NTCR thermistors are recognized for their high sensitivity (characterized by the thermal constant β) and resistivity. Such features make them particularly effective for remote applications, where high resistance minimizes the influence of lead wires on measurement accuracy, thus allowing for a simplified two-point measurement setup through a simple voltage divider circuit [6,7]. Despite their advantages, NTCR thermistors face significant challenges, such as limited operational temperature range (typically below 300 °C) and self-heating effects at higher temperatures [6]. In fact, these materials often become conductive at high temperatures [8] or exhibit different conduction mechanisms throughout the temperature range [9], which limits their utility. As their high sensitivity results in a wide resistance span between the highest and lowest

---

* Corresponding author at: IPN - LED&MAT - Instituto Pedro Nunes, Laboratório de Ensaios, Desgaste e Materiais, Rua Pedro Nunes, Coimbra 3030-199, Portugal.
E-mail address: brunomartins@ipn.pt (B. Martins).

https://doi.org/10.1016/j.jallcom.2025.178546
Received 24 August 2024; Received in revised form 16 December 2024; Accepted 7 January 2025

temperature, there is a lack of consensus regarding the optimal β values for high-temperature operations. While some researchers believe that thermistors should have high β values [5,9], others suggest that lower β values are more suitable for such conditions [10,11]. Moreover, traditional manufacturing techniques for these thermistors primarily involve powder technology. This process produces bulk semiconductors, posing substantial challenges in miniaturization and surface integration.

On the other hand, thin film sputtering techniques have shown promising advances regarding the development of oxide thermistors. However, they also reflect the limitations observed in sensors produced by powder-based methods, i.e., their inability to measure high temperatures [14,15].

Regarding the use of nitrides, notable progress has been made in integrating aluminum into stable transition metal nitrides, such as titanium nitride (TiN) and zirconium nitride (ZrN). The substitution of Ti or Zr by Al facilitates the formation of metastable solid solutions that exhibit superior wear and oxidation resistance [3,14,15]. While $Ti_{1-x}Al_xN$ forms a face-centered cubic (fcc) solid solution up to $x \approx 0.6–0.7$ [16,17], $Zr_{1-x}Al_xN$ also exhibits similar alloying mechanisms but for lower aluminum contents ($x \approx 0.3–0.4$) [3,18]. The thermomechanical properties of TMNs, including TiAlN and ZrAlN, are well-documented, establishing their suitability for wear applications. Beyond these properties, prior research has demonstrated that TMNs also exhibit NTCR behavior, making them promising candidates for temperature sensors [17,19–21]. For instance, $Ti_{1-x}Al_xN$ has been shown to exhibit NTCR behavior with a β value of approximately 1600 K for compositions ranging from $0.21 \leq x \leq 0.56$ [17,19]. Similarly, $Zr_{1-x}Al_xN$ demonstrates NTCR properties for $x \leq 0.34$ with a β value of approximately 2600 K [22]. Despite these findings, the potential of ZrAlN to function as a high-temperature sensor remains unexplored. While previous studies have investigated the electrical properties of ZrAlN as a function of Al concentration [20,24,25], its capacity to function effectively as a sensor at high temperatures, such as TiAlN [21], have not been evaluated so far.

To address this limitation, this study investigates the deposition of a ZrAlN thermistor sensor integrated into a multilayer coating system, incorporating insulator layers of aluminum nitride (AlN) and a TiAlN wear-resistant layer for electrical shielding and mechanical protection, respectively. The multilayer coating, produced via magnetron sputtering, follows the architecture and patterning strategy outlined by Martins et al. [21]. The thermistor layer was developed based on the findings previously reported by the current authors [22], and its operational capacity was verified up to 750 °C, demonstrating its potential in high-temperature applications. The thermistor layer, integrated into the full nitride multilayer coating on a traditional cutting tool substrate and calibrated up to 400 °C, highlights its utility in measuring the temperature in cutting operations.

2. Experimental methods

2.1. Deposition strategy for the ZrAlN sensor layer

The ZrAlN active layer was embedded between AlN insulator films, and the entire assembly was encapsulated by a TiAlN coating for enhanced wear resistance. The multilayer coating was deposited using a single magnetron sputtering unit equipped with four sputtering targets arranged in a closed-field magnetic configuration: two targets of zirconium and two of aluminum. As mentioned before, the layering architecture was strategically developed to provide electrical insulation and wear protection. The detailed process steps and parameters, except those for the ZrAlN layer, are summarized in our previous work for TiAlN-based sensors [21].

According to previous results [22], it is possible to attain a face-centered-cubic (fcc) $Zr_{1-x}Al_xN$ film exhibiting NTCR thermistor behavior for $x \approx 0.26$. The deposition conditions for the sensor layer are summarized in Table 1, which includes two sets of parameters tailored to achieve the desired chemical composition of the ZrAlN layer. The selected configuration of ZrAlN, designated as $ZrAlN_2$ in Table 1, was embedded within the multilayer coating to effectively coat the cutting tool substrate. As will be demonstrated during the study, $ZrAlN_2$ proved to be more stable under operational conditions than $ZrAlN_1$.

Table 1
Deposition conditions used to deposit the single ZrAlN temperature sensor.

Ultimate vacuum (Pa)	$< 5 \times 10^{-4}$	
Substrates in-situ cleaning – physical etching		
Substrate bias (V)	− 300	
Time (min)	15	
Ar pressure (Pa)	0.1	
Targets power density ($W \cdot cm^{-2}$)	0.15	
Pulse frequency (kHz)	245	
Reverse time (μs)	1.8	
Deposition procedure		
	$ZrAlN_1$	$ZrAlN_2$
Gas mixture ratio (N_2/Ar)	1.4	1.6
Working pressure (Pa)	≈ 0.25	≈ 0.25
Table speed (RPM)	1	
Satellite speed (RPM)	5	
Al Power density ($W \cdot cm^{-2}$)	≈ 1.6 (× 2)	≈ 1.9 (× 2)
Zr Power density ($W \cdot cm^{-2}$)	≈ 5.5 (× 2)	≈ 5.5 (× 2)
Substrate bias (V)	−40	
Bias pulse frequency (kHz)	250	
Bias reverse time (μs)	0.5	
Deposition time (min)	60	
Target-substrate distance (mm)	100	
Substrate temperature (°C)	≈ 200	

2.2. Characterization of the ZrAlN single layer

The electrical resistance variation of ZrAlN sensors (deposited on a sapphire substrate) with temperature changes was evaluated using both four-point (4PM) and two-point (2PM) measurement methods under vacuum conditions, to prevent surface oxidation. The 4PM was conducted with an Ossila four-point probe instrument, designed to measure sheet resistance from $100\ m\Omega \cdot sq^{-1}$ to $10\ M\Omega \cdot sq^{-1}$: it was connected to a temperature assessment bench equipped with a SiC heater (proportional – integral – derivative) PID controlled, and the measurements were taken using four gold-coated tungsten probes. Measurements were taken at 50 °C increments up to 750 °C during the heating cycle. The temperature bench was equipped with two calibrated thermocouples: one to regulate the SiC heater for precise temperature control and the other to measure the reference temperature. The Ossila Sheet Resistance V2.0.7.1 software automatically applied correction factors to account for the sample's geometric parameters [24]. The 2PM method was used to complement the 4PM method findings, using a high-resolution multimeter to monitor the resistance variations at a rate of 10 samples per second. These measurements helped validate the stability and repeatability of the patterned sensor's response across different thermal cycles, from room temperature to 400°C.

The thermal index β and temperature coefficient of resistance (TCR) were calculated over a defined temperature range (50–200 °C). In particular β, it was calculated based on the following expression:

$$\beta_{[50-200\ ^\circ C]} = \frac{\ln\left(\frac{R_{T1}}{R_{T2}}\right)}{\left(\frac{1}{T_1} - \frac{1}{T_2}\right)} \tag{1}$$

where β is in K, and R_{T1} and R_{T2} represent the sheet resistance at temperatures T_1 and T_2, respectively. The TCR was computed within the same temperature range using the expression:

$$TCR = \frac{R_2 - R_1}{R_1 (T_2 - T_1)} \tag{2}$$

where TCR is in K^{-1}.

The sensor's morphology and chemical composition were examined using a ZEISS Merlin® FE-SEM equipped with an EDX system from Oxford Instruments. The crystal structure was analyzed using X-ray diffraction (XRD) on Rigaku® system with a Cu Kα radiation ($\lambda = 0.154056$ nm) source. The XRD patterns were fitted using a Pseudo-Voigt function for peak deconvolution and position, and for determination of the full width at half maximum (FWHM). Joint Committee on Powder Diffraction Standards (JCPDS) cards were used for peak identification: ZrN 74-1217; Zr_3N_4 87-0843; Zr_2N 46-1204. The interplanar spacing d_{hkl}-spacing was calculated using Bragg's law formula.

2.3. Characterization of the ZrAlN single layer integrated into the multilayer coating

To elucidate the spatial distribution of elements throughout the multilayer coating and to assess the microstructural properties of the ZrAlN sensing layer, various electron microscopy techniques were employed. A lamella (5 µm × 4 µm × 0.1 µm—length × depth × thickness) of the coating, prepared using a Dual Beam FIB-SEM (FEI Helios NanoLab 450S), facilitated detailed cross-sectional analysis. This preparation methodology allowed for electron-transparent specimens (≤ 100 nm thickness) suitable for examination via Scanning Transmission Electron Microscopy (STEM) and Energy Dispersive X-ray Spectroscopy (EDX), which were carried out in a FEI Titan G3 Themis Cubed (X-FEG) transmission electron microscope, operated at 200 kV and equipped with Cs DCOR probe corrector and Super-X EDX system. Crystallographic information was obtained by selected area electron diffraction (SAED) technique. TEM Imaging and SAED characterization was performed in a FEI Titan G2 ChemiSTEM (FEG) transmission electron microscope, operated at 200 kV and equipped with a CCD camera Gatan UltraScan 1000XP (Model 994) 2k × 2k pixels. The combination of STEM, EDXS, TEM and SAED allowed for precise characterization of the ZrAlN layer's integration and its elemental composition within the multilayer architecture.

The electrical resistance variation of the multilayer coating in response to temperature changes was assessed using the same two-point measurement (2PM) method, as employed for the single-layer deposited on the sapphire substrate. Calibration involved conducting four temperature cycles between ambient temperature and 400 °C, with heating rates of 20 °C/min and natural cooling. The curve fitting was done using the Eq. (1) considering the resistance value at room temperature (R25). This calibration, performed under vacuum to prevent oxidation of the TiN layers and tungsten carbide (WC) substrate, was necessary for ensuring operational stability and performance of the ZrAlN layer within the sensor's architecture.

Following calibration, the operational stability and accuracy of the multilayer coating were further tested at a constant temperature of 100 °C for 10 min in air, to verify its accuracy and reliability. Signal acquisition was managed using an Arduino® Nano 33 IoT board with a voltage divider setup using a reference resistor of 200 kΩ. This setup tested the accuracy of the complete system (multilayer coating plus acquisition system).

3. Results and discussion

3.1. ZrAlN sensor layer structural and chemical analysis

The ZrAlN single layer deposited on the sapphire substrate was analyzed by SEM-EDX before the sheet resistance experiments, and the chemical composition for the $ZrAlN_1$ and $ZrAlN_2$ samples is presented in Table 2. As mentioned in the experimental methods section, the goal was to achieve a chemical composition in close agreement with previously published results for $Al/(Al + Zr)$ ratio ~ 0.26 [17], where such composition has been shown to provide sensor properties.

Table 2
Chemical composition for $ZrAlN_1$ and $ZrAlN_2$ samples as-deposited, taken at 10 keV.

	Zr (at%)	Al (at%)	N (at%)	O (at%)
$ZrAlN_1$	29.9 ± 0.1	9.9 ± 0.1	57.5 ± 0.3	2.7 ± 0.4
$ZrAlN_2$	27.5 ± 0.2	11.5 ± 0.1	58.5 ± 0.3	2.5 ± 0.5

Fig. 1 depicts the XRD patterns for samples $ZrAlN_1$ and $ZrAlN_2$, from 30° to 50°, as no relevant peak is observed above 50°. In Fig. 1(a), the XRD spectrum of $ZrAlN_1$ (displayed in green) exhibits three prominent peaks arranged from lower to higher angles. The first is a broader peak corresponding to the poorly crystallized phases of ZrN (with further details provided in Fig. 1(b)). The second peak, visible at 39.3°, is attributed to the (200) plane of the ZrAlN cubic phase, while the third peak is assigned to the substrate. The shift of the (200) plane to higher angles relative to the standard ZrN (200) position indicates a contraction of the unit cell, consistent with the substitution of Zr by the smaller Al atom in the ZrN fcc lattice. This substitution is further evidenced by the (111) plane identified by the peak at 33.7° (refer to the square labeled peak in Fig. 1(b) for $ZrAlN_1$), which is also shifted to higher angles, suggesting a systematic reduction of the lattice. This substitution corroborates findings from other studies that document a systematic structural evolution in ZrAlN coatings, with increased aluminum incorporation [18,23,25,26]. In addition, the broad peak deconvoluted in Fig. 1(b) for $ZrAlN_1$ includes additional peaks such as the (320), (201), and (140) planes of nitrogen-rich Zr_3N_4 phase at 32.1°, 33.2°, 34.4°, respectively, and the nitrogen-deficient Zr_2N phase at 35.9°. The appearance of Zr_3N_4, a ZrN metastable phase typically nitrogen-rich [27,28], may result from the interstitial incorporation of excess nitrogen, resulting in lattice expansion. The small peak representing the Zr_2N phase is likely attributable to a brief nitrogen supply fluctuation during the deposition process, lasting approximately 60 seconds; a temporary deviation in the nitrogen-to-argon ratio could have locally favored the formation of this phase.

As the aluminum content increases in the $ZrAlN_2$ sample, an intense, asymmetric, and broader peak profile appears (refer to diffraction pattern in Fig. 1(b) $ZrAlN_2$). This peak contains two poorly crystalline phases of Zr_3N_4 and ZrAlN, represented by the (320), (201), (140) and (111) planes, and positioned at 32.2°, 33.2°, 34.4° and 33.9°, respectively. The increase in the aluminum content causes a slight shift of the (111) peak to higher angles and the absence of a distinct (200) one. The (111) peak shift highlights the continuous reduction of unit cell dimensions due to the substitution of the Zr, suggesting that Al is still completely soluble in the cubic ZrN lattice. The absence or decrease of the (200) peak intensity with increasing Al is typically found in other studies [2,3,15,29,30] and can be explained by the lattice distortion caused by the increase of the Al content. The (111) plane in the fcc structure can better accommodate distortions without increasing lattice strain energy. Moreover, the increased formation of the Zr_3N_4 phase may also be related to the distortion promoted by the increased Al content in the mixture, as this can facilitate higher nitrogen incorporation in the ZrN lattice [28,30,31]. This structural evolution is followed by the nitrogen content measurements presented in Table 2, showing higher nitrogen levels in $ZrAlN_2$. While $ZrAlN_1$ and $ZrAlN_2$ exhibit different structural characteristics, both demonstrate a mixture of cubic and orthorhombic defect-rich phases.

3.2. Electrical characterization of ZrAlN sensor

Fig. 2 presents the sheet resistance response to temperature variations for $ZrAlN_1$ (Fig. 2(a)) and $ZrAlN_2$ (Fig. 2(b)), illustrating typical semiconductor behavior with a decrease in the resistance upon heating, emphasizing their potential for temperature sensing [32]. Despite the consistent behavior across runs, the initial variability in R25 highlights the need for electrical signal stabilization, a common requirement in oxide thermistors [12,13].

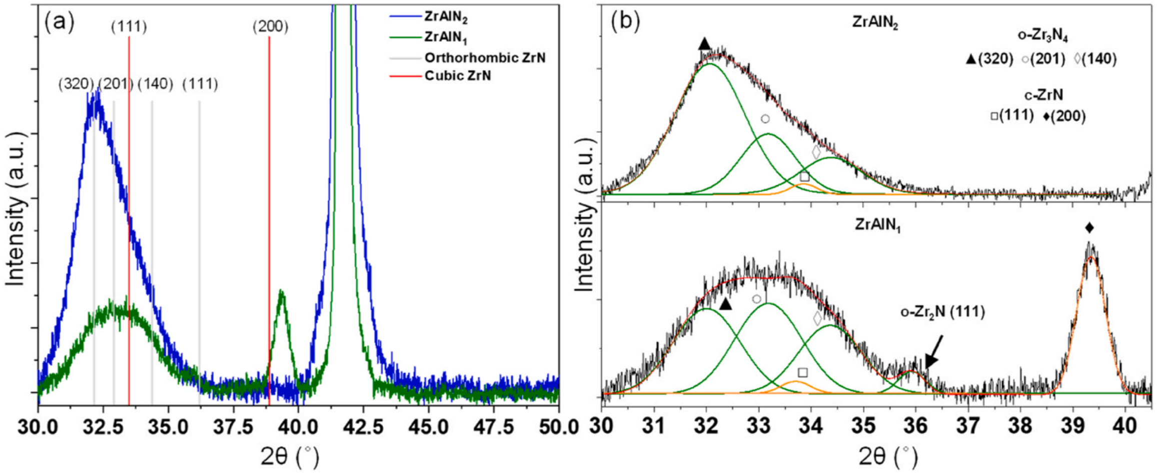

Fig. 1. As-deposited X-ray diffraction patterns of ZrAlN$_1$ and ZrAlN$_2$ on sapphire substrates, from 30° to 50°: (a) XRD patterns for ZrAlN samples deposited at different target powers, 1000 W for ZrAlN$_1$ (green pattern) and 1200 W for ZrAlN$_2$ (blue pattern), in which the red and silver lines correspond to cubic and orthorhombic phases of ZrN, respectively; (b) peak deconvolution for the ZrAlN$_1$ and ZrAlN$_2$ samples and respective phases associated (Standard ICDD card numbers used – ZrN 74-1217, Zr$_3$N$_4$ 87-0843, and Zr$_2$N 46-1204).

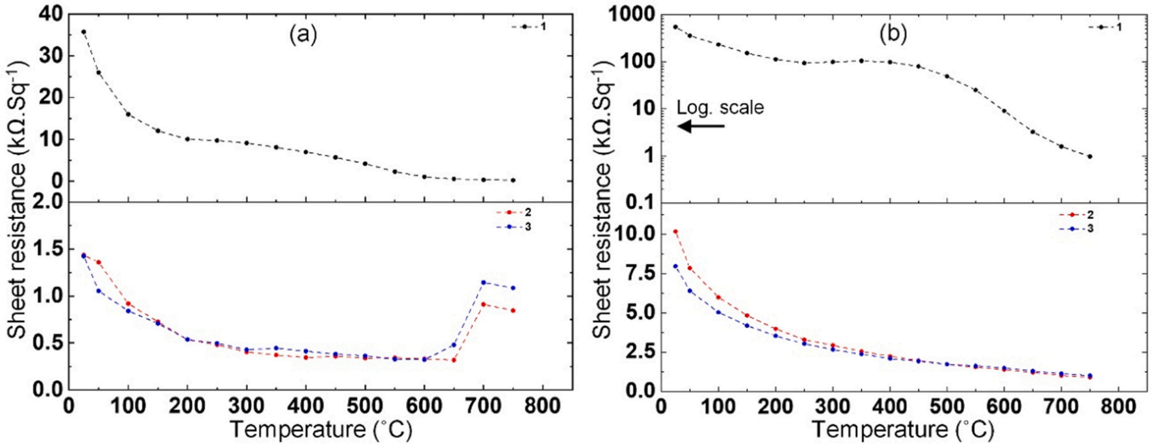

Fig. 2. Temperature-dependent sheet resistance of ZrAlN coatings: (a) displays the sheet resistance as a function of temperature for three successive runs of the ZrAlN$_1$ sample; (b) illustrates the sheet resistance of the ZrAlN$_2$ sample, also across three runs, on a logarithmic scale to highlight the nonlinear response for the first run.

For ZrAlN$_1$, sensitivity decreases markedly from 971 to 686 K by the third run, in agreement with the decrease observed on TCR and resistivity, stabilizing at 1.4×10^5 μΩ·cm and -3.3×10^{-3} K^{-1}, respectively. Interestingly, there is a shift towards metallic behavior above 650 °C, likely due to the increased Zr content in the compound, resulting in a higher availability of charge carriers. The shift can be explained by the saturation of charge carriers in the extrinsic region and their hindered mobility due to the temperature effect, phenomena previously observed in nitride studies at lower temperatures [17,22]. The ZrAlN$_2$ follows the same trend, with sensitivity, TCR, and resistivity stabilizing at 607 K, -3.0×10^{-3} K^{-1}, and 8.0×10^5 μΩ·cm, respectively. Unlike ZrAlN$_1$, ZrAlN$_2$ maintains stable electrical properties without transitioning to metallic behavior, indicating its reliability for continuous high-temperature operation.

Both samples exhibit lower β and TCR values than those reported by Martins et al. [22], albeit with higher resistivity. Since the authors did not specifically focus on signal stabilization in their study, it is challenging to make direct comparisons. The discrepancies in resistivity compared to other studies [1,18,25] may be due to the nitrogen-rich phase detected by XRD, known for its high electrical resistivity [27,28,31]. It is generally agreed that the distortion of the cell resulting from the high nitrogen inclusion reduces the metallic properties of the ZrN bond [28,31] and the availability of free electrons [27]. The orthorhombic phase is more pronounced in ZrAlN$_2$, as depicted in Fig. 1(a), contributing to its higher electrical resistivity. In addition, the poor crystallinity of the samples could be responsible for hindering the flow of charge carriers, further increasing the resistivity [22]. Both samples align well with the performance of conventional platinum resistance temperature detectors (RTDs) [7] despite having lower TCR values than those of typical oxide thermistors [5]. This suggests their suitability for precise measurements across a broad range of temperatures.

The debate in the literature about optimal β values for high-temperature applications reflects conflicting views. Fujita et al. [19] claimed that materials with β below 1000 K pose challenges for thermistor applications; however, they also recognized the need for low β values to measure broader temperature ranges [10]. High sensitivity is necessary for detecting minor temperature variations, but the associated exponential resistance decay complicates the accuracy of high-temperature readings due to low resistance levels. Furthermore, high sensitivity often comes with high resistivity [5], which makes it more complicated to handle low-bias currents. Although there is no general agreement on this topic, the lower β values observed in this study proved advantageous for capturing high temperatures. This finding demonstrates that, unlike traditional thermistors, which face limitations at elevated temperatures [8,12,33], our sensor keeps its stability and acceptable resistance values across a wide temperature range, making it well-suited for integration into electronic systems.

3.3. Electrical stabilization of ZrAlN sensor

The electrical stabilization was evaluated using a ZrAlN synthesized under the $ZrAlN_2$ process conditions detailed in Table 1, chosen for its stable electrical response during prior sheet resistance measurements. Fig. 3(a) depicts the changes in electrical resistance of the ZrAlN temperature sensor deposited on a sapphire substrate as it undergoes thermal cycling. The sensor design presented in Fig. 3(b) aimed to lower the electrical resistance of the sensor, since it exhibits a sheet resistance in the kΩ range [5]. Still, the full-length composition of ZrAlN in the sensor path led to resistance values in the MΩ range. Introducing a conductive material path could potentially lower the resistance; however, this modification would require additional deposition steps and create more interfaces. Compared to other approaches, such as thermocouples requiring two dissimilar materials and masking steps [34,35], our single-material thin-film sensor simplifies the integration process. This advantage is especially relevant for industrial applications where scalability and cost-efficiency are critical.

During the temperature cycles extending from room temperature to 300 °C in vacuum, the sensor exhibited a decrease in resistance with increasing temperature, consistent with the NTCR behavior typical of semiconductors. However, an increase in resistance was observed during the holding step at 300 °C, suggesting instability. As Ferreira et al. [36] have noted in a similar study on resistive film sensors, achieving signal stabilization often needs thermal treatment at low temperatures to address factors like grain refinement, growth, and recrystallization, which can influence the sensor's performance. In this case, the observed resistance increase is attributed to stress accumulation within the ZrAlN film, prompted by thermal expansion and subsequent contraction. Upon cooling, the resistance values tend to stabilize, indicating a structural relaxation of the film's microstructure, which adjusts to accommodate changes in the substrate's dimensions. Similar behavior was noted in the prior study using TiAlN sensors [21], where significant resistance fluctuations are addressed by post-deposition annealing to ensure reliable temperature readings.

Fig. 4(a) illustrates the resistance behavior of the ZrAlN film during temperature cycles between 300 and 400 °C in vacuum. Notably, the resistance stabilizes significantly after maintaining the temperature at 400 °C for approximately 15 min, with a ΔΩ of approximately 2000 Ω (0.2 % full range). This stabilization suggests that thermal treatment under these conditions enables the film to fully relax, thereby mitigating any residual stresses that might impact its electrical properties. Such treatment is readily achievable in situ with modern Physical Vapor Deposition (PVD) equipment, capable of heating substrates up to 600 °C (not feasible in our PVD apparatus).

Fig. 4(b) shows the results of the resistance-temperature experiment post-signal stabilization, highlighting the absence of hysteresis between the heating and cooling curves. The calculated sensitivity and TCR are approximately 850 K and $-4.0 \times 10^{-3}\ K^{-1}$, respectively, indicating an improvement from the earlier observations (see Fig. 2). This improvement emphasizes the efficacy of the thermal treatment in enhancing the sensor's performance. Although the sensitivity of the nitride film sensor does not reach the levels typically seen in conventional thermistor sensors, its relatively low sensitivity implies a near-linear resistance response to temperature changes. This characteristic aligns with the growing demand for linear thermistors [33], offering a reliable solution for applications requiring straightforward calibration and broad temperature measurement ranges.

3.4. Morphological, structural and electrical characterization of ZrAlN layer in multilayer coatings

After analyzing the structural and electrical characteristics of the ZrAlN layer, Fig. 5 highlights the complexity involved in embedding such sensors within multilayer coatings. Fig. 5(a) shows a high-angle annular dark-field (HAADF)-STEM cross-sectional view of the multilayer architecture deposited over the cutting insert. Fig. 5(b) shows the ZrAlN layer in greater detail, where the presence of voids, labeled as "1", is indicative of growth defects common in PVD processes. These defects, which may have arisen from suboptimal adatom mobility due to low substrate bias and lack of heating during deposition, undermine the density and continuity of the columnar structures [37]. In fact, defects such as voids and cracks can interrupt the continuity of the film, resulting in electrical resistance and signal fluctuations. In addition, they can hinder charge carriers movement [21], potentially leading to electrical failure. For instance, some samples did not function as sensors due to low electrical resistance (~ 10 Ω).

Although intermediate ion etching steps were employed to enhance layer interlocking – a strategy derived from established protocols [21] – they were not effective in disrupting the formation of voids between the

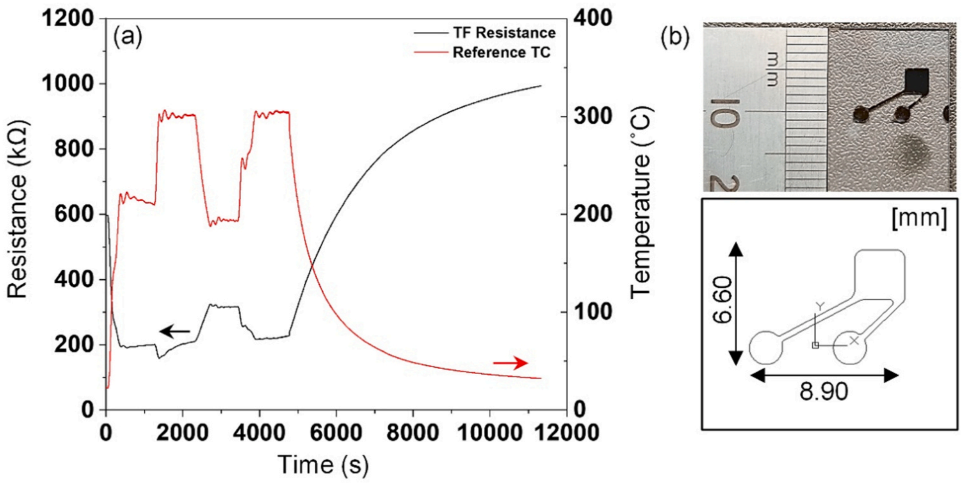

Fig. 3. Thermal cycling and ZrAlN thin film sensor design. (a) Resistance (black line-TF) versus time for a ZrAlN sensor subjected to thermal cycling in vacuum, alongside a reference thermocouple temperature curve (red line-TC); (b) Top inset – image of the ZrAlN sensor deposited on a sapphire substrate, illustrating the physical placement and size of the sensor, bottom inset – schematic of the sensor layout, showing the global dimensions and orientation of the sensor on the substrate.

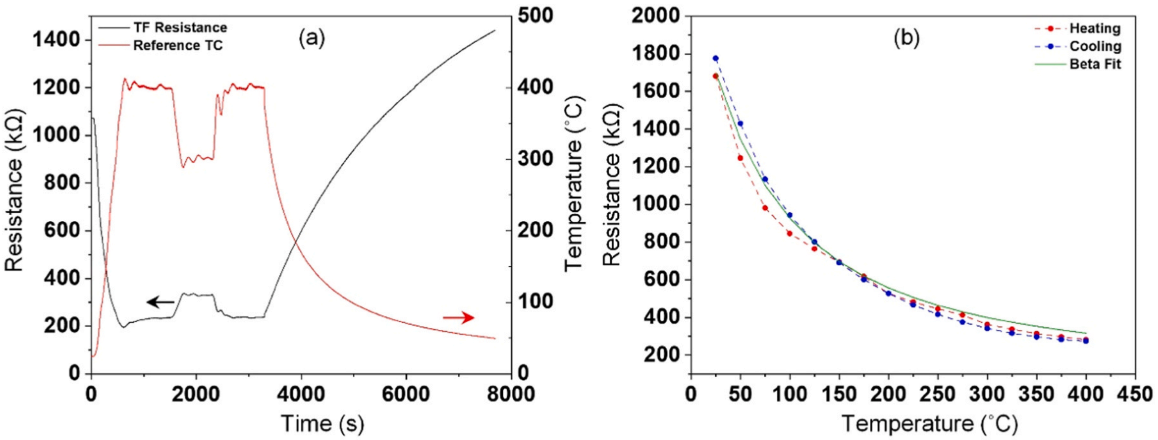

Fig. 4. Thermal cycling and resistance stabilization of the ZrAlN thin film sensor in vacuum. (a) Resistance (black line-TF) versus temperature (red line-TC) thermal cycling from room temperature to 400 °C; (b) resistance versus temperature after thermal stabilization, heating (red dash-dot line) and cooling (blue dash-dot line) cycles, overlaid with a β fit curve (green line).

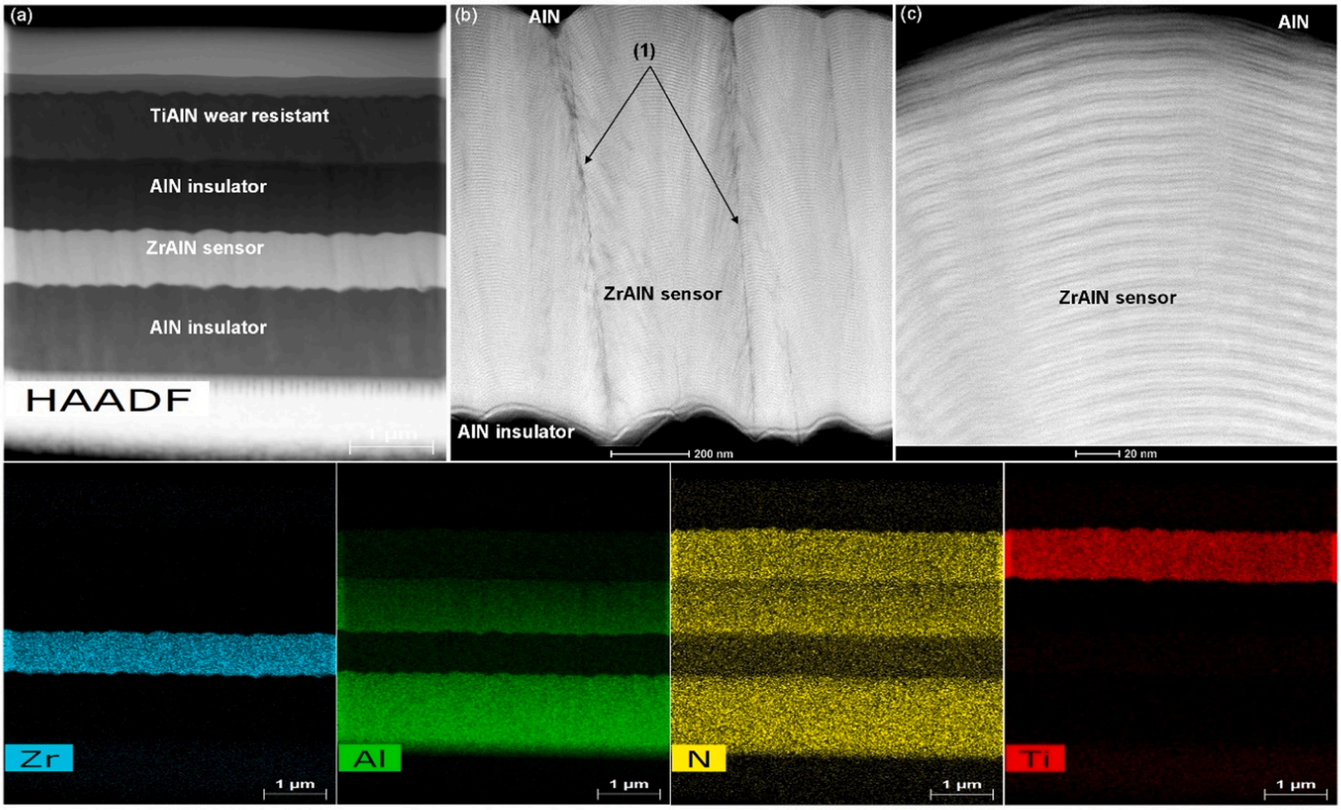

Fig. 5. HAADF – STEM images of the multilayer coating deposited on WC-Co substrate focusing the ZrAlN sensor layer, with the respective EDX maps (bottom images) revealing the elemental distribution of Al, Ti, Zr, and N along the thickness: (a) multilayer coating architecture; ZrAlN layer from lower (b) to higher magnification (c), where label 1 indicates the presence of growing defects in the ZrAlN layer (the FIB cut - lamella - was performed in the cutting tool).

columnar grains. The presence of this type of defect suggests a need for further optimization of deposition parameters, particularly those influencing adatom energy and substrate interactions such as bias voltage or working pressure. Nevertheless, since Martins et al. [22] demonstrated the importance of grain size and grain boundaries in the conduction mechanism in ZrAlN, the effect of these parameters on the electrical properties should not be ignored.

Despite the waviness pattern of the multilayer coating (Fig. 5(a)), there is a continuous growth of the sensor columns (see Fig. 5(b)). Upon closer examination of the embedded ZrAlN sensor through Fig. 5(b) and Fig. 5(c), a distinct multilayer structure with alternating light and dark contrasts is visible, including nanometer-thin sublayers. This arrangement reflects the layering achieved by simultaneous sputtering from Zr and Al targets, combined with the motion of the substrate in the chamber. The alternating light and dark bands in the ZrAlN sensor corresponding to Al-poor and Al-rich zones (label 1), as depicted in the EDXS maps shown in Fig. 6, suggesting that the ZrAlN film alternates between a fcc and the orthorhombic phase.

The two-fold rotation mode, commonly utilized in the manufacture of cutting tools, and replicated in this study, plays an essential role in the

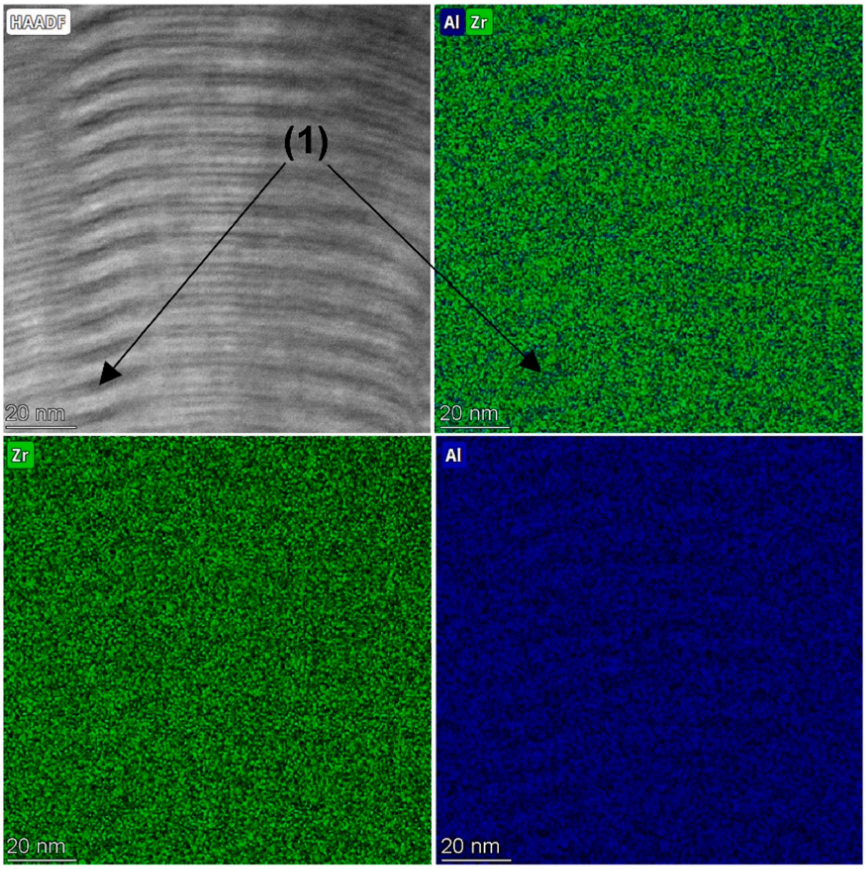

Fig. 6. Detailed high-angle annular dark-field STEM image of the sensor layer ZrAlN with the respective EDX Spectroscopy maps. EDXS maps show the elemental spatial distribution of Al and Zr elements and their respective overlap. Label 1 indicates an Al-rich zone in the map distribution and the corresponding site in the HAADF image.

industry to achieve uniform coatings over complex geometries. However, once the substrates passes through varying plasma zones, intricate multilayer layers are formed [30,38,39], as occurred in our setup. Additionally, this movement could cause the shadowing effect of the incoming atomic flux, leading to preferential deposition of adatoms on the tops of the growing columns resulting in sharp columnar boundaries. During the heating phase, the film's elongation could potentially expand the gaps between these columns, adversely affecting the electrical conductivity. Conversely, during the cooling phase, the film undergoes a relaxation process that tends to narrow those gaps, thereby stabilizing the electrical signal. This dynamic process is believed to occur during signal stabilization in thermal experiments.

Fig. 7(a) shows a bright-field TEM micrograph of the ZrAlN layer, including an inset showing the corresponding SAED pattern. The interplanar spacings (d_{hkl}) measured from the diffraction rings displayed in Fig. 7(b) match with those indexed for ZrN (ICDD file 74-1217) and Zr_3N_4 (ICDD file 87-0843), indicating the possible presence of these phases within the layer. The SAED patterns identify the crystallographic planes of ZrN, namely the (111), (200), (220), and (320), (201), (140) planes for the Zr_3N_4 phase. The broader first ring, containing both the

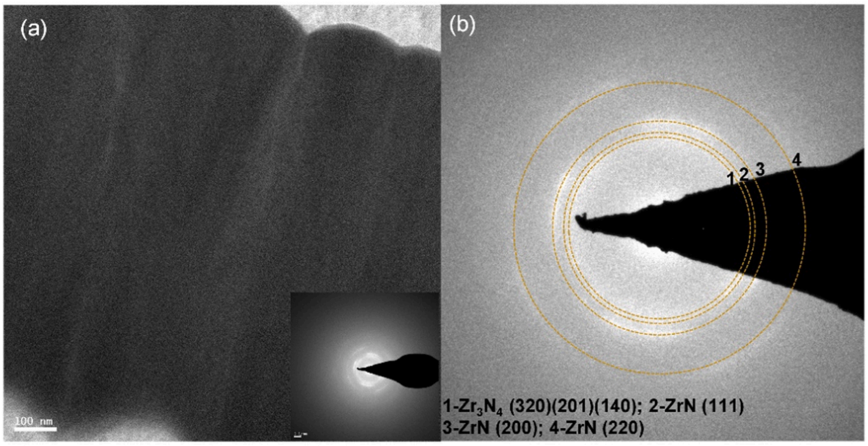

Fig. 7. (a) Bright-field TEM image of a ZrAlN thin film. The inset shows the corresponding SAED pattern; (b) Detailed view of the SAED pattern, showing the diffraction rings that identify the phases present in the ZrAlN system.

ZrN-(111) and Zr_3N_4 phases (corresponding planes have close d_{hkl}), supports the XRD discussion, suggesting a mixture of these phases. The diffuse nature of the rings, indicative of weak crystallinity, further corroborates the XRD analysis and the conclusion that ZrAlN is mainly composed of Zr_3N_4 and ZrN phases.

3.5. Temperature sensor functionality of the multilayer coating integrating the ZrAlN sensor layer

The practical application of the multilayer coating for temperature measurements in cutting tools was explored in this study using a popular electronics platform (an Arduino board) to facilitate signal processing. Initial experiments focused on stabilizing the sensor's signal; the coated cutting tool was subjected to a temperature of 400 °C for 20 min in vacuum to prevent oxidation, during which time its resistance was continuously monitored.

As depicted in Fig. 8(a), the resistance decreases as the tool reaches the maximum temperature and stabilizes approximately 10–15 min after reaching the holding step of 400 °C. As discussed above, this stabilization phase is critical for ensuring reliable temperature readings, which is why it was conducted under vacuum conditions to mitigate TiN contacts and tungsten carbide (WC) substrate oxidation risks. The design shown in the inset features a cutting tool coated with a sensitive multilayer coating. The TiN is positioned away from high-temperature areas where the tool and workpiece get in contact, so it is not prone to oxidation under normal operating conditions [34]. Furthermore, the layered design, incorporating protective AlN and TiAlN, shields the ZrAlN sensor from oxidation, ensuring its durability and performance in high-temperature environments typical of metal-cutting operations.

Fig. 8(b) illustrates the result of four heating-cooling cycles after stabilization, confirming the sensor's behavior robustness. The calculated sensitivity closely matches what was observed with the single-layer sensor tests after thermal stabilization. The application of a β fitting simplifies the calibration process, though it introduces a minor measurement uncertainty, particularly near 400 °C, where a slight deviation is observed. Additionally, the observed variability in R25 values across different samples can be managed effectively due to minor fluctuations in the β value, minimizing the need for recalibration. This adaptability offers a significant advantage over thin-film thermocouples [34,35], where such flexibility is less straightforward to achieve. The R25 variability may be linked to structural inconsistencies like intercolumnar voids observed in cross-sectional analyses, which can introduce paths for electrical short-circuits, particularly after incorporating conductive TiN layers. Despite these limitations (also found in the multilayer coating study using TiAlN as sensor layer [21]), the cutting tool demonstrated stability, making it well-suited to measure temperature in high-temperature applications such as metal cutting or high-speed machining.

Fig. 9 shows the temperature response results of the system, the multilayer coating combined with the Arduino board-based acquisition system. In the experiment, conducted up to 100 °C, the system error was computed, and its functionality as a temperature sensor was confirmed. Fig. 9(a) illustrates the behavior of the sensor and the resulting TC from the PID-controlled heating steps until it reaches and holds at 100 °C. Despite the multilayer coating effectively managing small temperature fluctuations, a slight deviation from the TC measurements was noted during the cooling phase, likely attributed to the higher thermal inertia of the cutting tool compared to the TC. This deviation decreases as a fan is positioned to cool the apparatus, aligning the sensor's signal more closely with the TC, thus highlighting the rapid response capability of the multilayer coating.

Fig. 9(b) details the simple yet effective signal acquisition system created for this experiment where is depicted the estimated error associated with the instrumentation. A 200 kΩ resistor was used as a reference resistor for the voltage divider without necessitating additional signal amplification, contrasting with our previous studies involving TiAlN, where signal amplification was necessary [21]. Adding a board with Wi-Fi connectivity highlights the system's utility for remote monitoring applications, eliminating the complexities associated with extensive wiring [34,35]. Unlike conventional approaches requiring high-resolution multimeters [8,12,33], our setup emphasizes the potential for real-time monitoring of inaccessible or challenging processes, leveraging the inherent advantages of thin-film technology. The sensor readings have an error of approximately 7 %, which is comparable to similar technologies discussed in the literature, such as the thin film thermocouples (TFTCs) examined by Lian et al. [35]. Their study documented higher error margins in temperature measurement during titanium cutting operations.

4. Conclusions

In this study, a nitride-based thermistor was successfully integrated within a multilayer coating designed for severe industrial applications, such as metal cutting, combining protective and sensing functionalities. The single-layer sensor demonstrates semiconductor behavior up to 750 °C, which can then be used as a high-temperature measuring device.

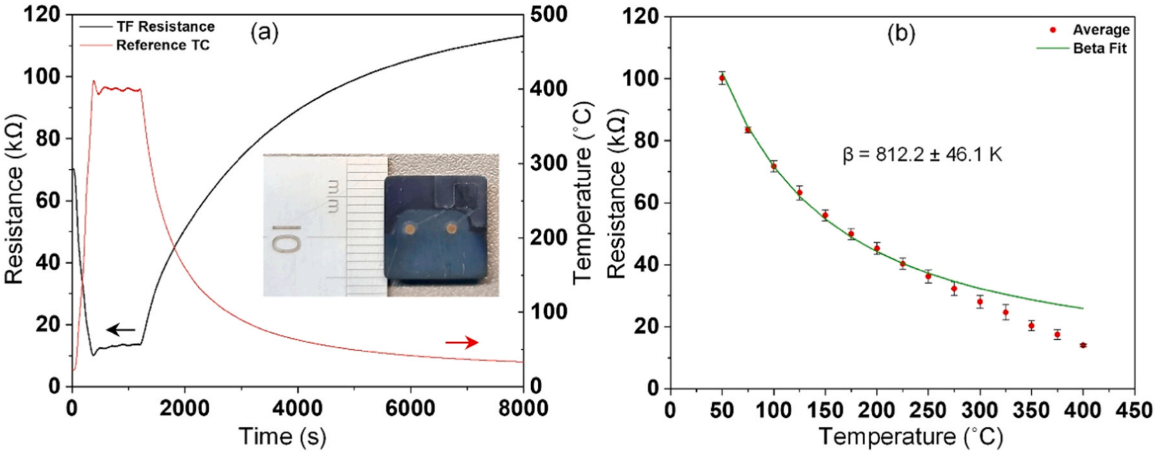

Fig. 8. Temperature-dependent electrical characterization of a ZrAlN sensor integrated into the multilayer coating on a cutting tool: (a) The resistance of the thin film (TF Resistance) plotted against the temperature profile measured by the reference thermocouple (Reference TC), holding the temperature of 400 °C over 20 min in a vacuum environment – the inset image highlights the arrangement of the sensor on the cutting tool substrate; (b) Resistance versus temperature response of the multilayer coating after signal stabilization (data points represent the average resistance at various temperatures, with the green line showing the β fit curve β = 812.2 ± 46.1 K - of the sensor's thermal response).

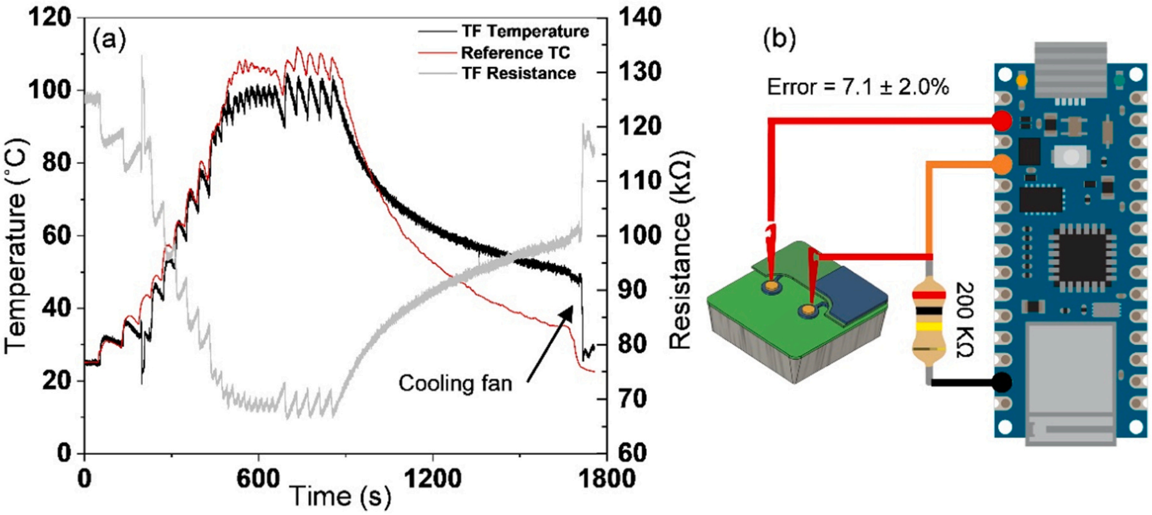

Fig. 9. System response and signal acquisition setup for the multilayer coating integrated with an Arduino® board: (a) temperature and resistance measurements obtained from the ZrAlN sensor integrated into the multilayer coating during thermal experiments conducted up to 100 °C in air – the plot shows the resistance (grey line) and the multilayer coating temperature (black line) acquired with the Arduino®, and temperature of the reference TC (red line); (b) Schematic illustration of the experimental setup, showing its connections to an Arduino® Nano 33 IoT board and demonstrating the configuration used for acquiring resistance and temperature data.

After signal stabilization, the material shows a consistent thermistor β value of approximately 850 K.

The structural analysis of $Zr_{0.7}Al_{0.3}N$ sensor revealed a unique combination of poorly crystalline Zr_3N_4 and ZrN phases alternating in aluminum content. The cross-sectional STEM analysis revealed a complex morphology of nanolayers modulation resulting from the two-fold rotational deposition process, commonly used in industrial applications. While common PVD growth defects, such as voids and intercolumnar separations, were identified, these defects did not significantly impact sensor stability up to 400 °C, with only a minor decrease in β. However, they may pose risks of electrical failure at higher temperatures, necessitating further optimization.

The signal acquisition system, comprising a simple 200 kΩ resistor and an Arduino board with a 12-bit analog-to-digital converter, demonstrated an overall measurement error of approximately 7 % at 100 °C. This configuration highlights the practicality and feasibility of integrating a ZrAlN thermistor within a multilayer coating for remote monitoring in various industrial applications. The simplicity of this single-material sensor design offers advantages over traditional thermistor fabrication methods, reducing the complexity and cost of manufacturing.

Future work will aim to extend our understanding of this multilayer architecture's performance and reliability at even higher operational temperatures, with a particular focus on monitoring temperature evolution in challenging environments, such as during the cutting of titanium alloys.

CRediT authorship contribution statement

Filipe Fernandes: Writing – review & editing, Validation, Supervision, Conceptualization. **Paulo Ferreira:** Writing – review & editing. **Cristiana Alves:** Investigation. **Enrique Carbo-Argibay:** Writing – review & editing, Investigation. **Pedro Faia:** Writing – review & editing, Investigation. **Albano Cavaleiro:** Writing – review & editing, Validation, Supervision, Conceptualization. **Carlos Patacas:** Visualization, Investigation. **Bruno Martins:** Writing – original draft, Visualization, Investigation.

Declaration of Competing Interest

The authors declare that they have no known competing financial interests or personal relationships that could have appeared to influence the work reported in this paper.

Acknowledgements

This research is sponsored by national funds: Soft4Sense Project "Smart Surfaces for Reliable Tooling Integration" (Reference: POCI-01-0247-FEDER-045921), co-financed by the European Regional Development Fund, through Portugal 2020 (PT2020), by the Competitiveness and Internationalization Operational Program (COMPETE 2020) and Foundation for Science and Technology (FCT) is also acknowledged. This research is also sponsored by national funds through FCT, under Projects UIDB/00285/2020 and LA/P/0112/2020. The authors also acknowledge the FCT for its financial support via the project LAETA Base Funding (https://doi.org/10.54499/UIDB/50022/2020), and the PRR Drivolution – Factory of the Future Model (reference: C644913740-00000022).

Data availability

Data will be made available on request.

References

[1] M. Magnuson, W. Olovsson, N. Ghafoor, M. Odén, L. Hultman, Interface bonding of Z r1-x A lx N nanocomposites investigated by X-ray spectroscopies and first principles calculations, Phys. Rev. Res. 2 (2020) 1–12, https://doi.org/10.1103/PhysRevResearch.2.013328.

[2] N. Ghafoor, I. Petrov, D. Holec, G. Greczynski, J. Palisaitis, P.O.A. Persson, L. Hultman, J. Birch, Self-structuring in Zr1−xAlxN films as a function of composition and growth temperature, Sci. Rep. - Nat. 8 (2018) 1–17, https://doi.org/10.1038/s41598-018-34279-w.

[3] L. Rogström, M.P. Johansson-Jõesaar, L. Landälv, M. Ahlgren, M. Odén, Wear behavior of ZrAlN coated cutting tools during turning, Surf. Coat. Technol. 282 (2015) 180–187, https://doi.org/10.1016/j.surfcoat.2015.10.029.

[4] Y.H. Chen, L. Rogström, J.J. Roa, J.Q. Zhu, I.C. Schramm, L.J.S. Johnson, N. Schell, F. Mücklich, M.J. Anglada, M. Odén, Thermal and mechanical stability of wurtzite-ZrAlN/cubic-TiN and wurtzite-ZrAlN/cubic-ZrN multilayers, Surf. Coat. Technol. 324 (2017) 328–337, https://doi.org/10.1016/j.surfcoat.2017.05.055.

[5] A. Feteira, Negative temperature coefficient resistance (NTCR) ceramic thermistors: an industrial perspective, J. Am. Ceram. Soc. 92 (2009) 967–983, https://doi.org/10.1111/j.1551-2916.2009.02990.x.

[6] P.R.N. Childs, J.R. Greenwood, C.A. Long, Review of temperature measurement, Rev. Sci. Instrum. 71 (2000) 2959–2978, https://doi.org/10.1063/1.1305516.

[7] L.H.J. Raijmakers, D.L. Danilov, R.A. Eichel, P.H.L. Notten, A review on various temperature-indication methods for Li-ion batteries, Appl. Energy 240 (2019) 918–945, https://doi.org/10.1016/j.apenergy.2019.02.078.

[8] D. Houivet, J. Bernard, J.M. Haussonne, High temperature NTC ceramic resistors (ambient-1000 °C), J. Eur. Ceram. Soc. 24 (2004) 1237–1241, https://doi.org/10.1016/S0955-2219(03)00376-5.

[9] B. Zhang, Q. Zhao, A. Chang, Y. Li, Y. Liu, Y. Wu, Spark plasma sintering of MgAl2O4-YCr0.5Mn0.5O3 composite NTC ceramics, J. Eur. Ceram. Soc. 34 (2014) 2989–2995, https://doi.org/10.1016/j.jeurceramsoc.2014.03.025.

[10] T. Fujita, K. Fujiwara, T. Yamaguchi, Electrical properties of La(Cr,Mn)O3 NTC materials, Key Eng. Mater. 485 (2011) 237–240, https://doi.org/10.4028/www.scientific.net/KEM.485.237.

[11] Y. Liu, B. Zhang, Z. Fu, A. Chang, New negative temperature coefficient ceramics in Ca0.9Y0.1MoO4–CeNbO4 system, Mater. Lett. 264 (2020) 127319, https://doi.org/10.1016/j.matlet.2020.127319.

[12] L. Ruifeng, Q. Fu, X. Zou, Z. Zheng, W. Luo, L. Yan, Mn-Co-Ni-O thin films prepared by sputtering with alloy target, J. Adv. Ceram. 9 (2020) 64–71, https://doi.org/10.1007/s40145-019-0348-y.

[13] T. Xuan, J. Yan, J. Wang, W. Kong, A. Chang, Characterization of Al-doped Mn–Co–Ni–O NTC thermistor films prepared by the magnetron co-sputtering approach, J. Alloy. Compd. 831 (2020) 154831, https://doi.org/10.1016/j.jallcom.2020.154831.

[14] X.Y. Zhu, J. Du, G.M. Liu, X.H. Zheng, Influence of Al-content on the microstructure and mechanical properties in ZrAlN coatings, Adv. Mater. Res. 1004–1005 (2014) 778–783, https://doi.org/10.4028/www.scientific.net/AMR.1004-1005.778.

[15] R. Franz, M. Lechthaler, C. Polzer, C. Mitterer, Oxidation behaviour and tribological properties of arc-evaporated ZrAlN hard coatings, Surf. Coat. Technol. 206 (2012) 2337–2345, https://doi.org/10.1016/j.surfcoat.2011.10.023.

[16] Y. Pinot, M.H. Tuilier, M.J. Pac, C. Rousselot, D. Thiaudière, C. Ulhaq-Bouillet, Influence of film thickness on the structural transition cubic/hexagonal within Ti0.38Al0.62N films, Thin Solid Films 649 (2018) 160–166, https://doi.org/10.1016/j.tsf.2018.01.024.

[17] B. Martins, C. Patacas, A. Cavaleiro, P. Faia, O. Bondarchuk, F. Fernandes, Electrical properties and thermistor behavior of TiAlN thin films deposited by combinatorial sputtering, Surf. Coat. Technol. 464 (2023) 129545, https://doi.org/10.1016/j.surfcoat.2023.129545.

[18] J. ping Meng, K. Zhang, X. peng Liu, Z. qiang Fu, Z. Li, Influence of the aluminum content on structure and optical properties of Zr1-xAlxN films, Vacuum 145 (2017) 268–271, https://doi.org/10.1016/j.vacuum.2017.08.045.

[19] T. Fujita, H. Tanaka, H. Inaba, N. Nagatomo, Development and electrical properties of wurtzite (Al,Ti)N materials for thin film thermistors, J. Ceram. Soc. Jpn. 124 (2016) 653–658, https://doi.org/10.2109/jcersj2.15316.

[20] M. Yoshikawa, D. Toyama, T. Fujita, N. Nagatomo, T. Makimoto, Hole conduction characteristics of cubic Ti1−xAlxN, Thin Solid Films 660 (2018) 711–714, https://doi.org/10.1016/j.tsf.2018.04.010.

[21] B. Martins, C. Patacas, A. Cavaleiro, P. Faia, F. Zorro, E. Carbo-argibay, P. J. Ferreira, F. Fernandes, Expanding the applications of the wear-resistant titanium aluminum nitride thin-film to include temperature sensing, J. Sci. Adv. Mater. Devices 9 (2024), https://doi.org/10.1016/j.jsamd.2024.100716.

[22] B. Martins, C. Patacas, A. Cavaleiro, P. Faia, O. Bondarchuk, F. Fernandes, Can ZrAlN thin films be used as thermistor sensors for temperature assessment, J. Sci. Adv. Mater. Devices 9 (2024) 100676, https://doi.org/10.1016/j.jsamd.2024.100676.

[23] G. Ke, Y. Tao, Z. He, H. Guo, Y. Chen, J. Dibattista, E. Chan, Y. Yang, Influence of sputtering atmosphere on crystal quality and electrical properties of zirconium aluminum nitride thin film, Surf. Coat. Technol. (2015), https://doi.org/10.1016/j.surfcoat.2015.09.046.

[24] I. Miccoli, F. Edler, H. Pfnür, C. Tegenkamp, The 100th anniversary of the four-point probe technique: the role of probe geometries in isotropic and anisotropic systems, J. Phys. Condens. Matter 27 (2015) 223201, https://doi.org/10.1088/0953-8984/27/22/223201.

[25] R. Lamni, R. Sanjinés, F. Lévy, Electrical and optical properties of Zr1-xAlxN thin films, Thin Solid Films 478 (2005) 170–175, https://doi.org/10.1016/j.tsf.2004.10.049.

[26] K. Yalamanchili, F. Wang, H. Aboulfadl, J. Barrirero, L. Rogström, E. Jiménez-Pique, F. Mücklich, F. Tasnadi, M. Odén, N. Ghafoor, Growth and thermal stability of TiN/ZrAlN: effect of internal interfaces, Acta Mater. 121 (2016) 396–406, https://doi.org/10.1016/j.actamat.2016.07.006.

[27] R. Lamni, E. Martínez, S.G. Springer, R. Sanjinés, P.E. Schmid, F.A. Lèvy, Optical and electronic properties of magnetron sputtered ZrN thin films, Thin Solid Films 447–448 (2004) 316–321, https://doi.org/10.1016/S0040-6090Ž03.01109-X.

[28] H.M. Benia, M. Guemmaz, G. Schmerber, A. Mosser, J.C. Parlebas, Investigations on non-stoichiometric zirconium nitrides, Appl. Surf. Sci. 200 (2002) 231–238, https://doi.org/10.1016/S0169-4332(02)00925-X.

[29] J.J. Araiza, O. Sánchez, J.M. Albella, Influence of the aluminum incorporation on the structure of sputtered ZrNx films deposited at low temperatures, Vacuum 83 (2009) 1236–1239, https://doi.org/10.1016/j.vacuum.2009.03.012.

[30] L. Rogström, M.P. Johansson, N. Ghafoor, L. Hultman, M. Odén, Influence of chemical composition and deposition conditions on microstructure evolution during annealing of arc evaporated ZrAlN thin films, J. Vac. Sci. Technol. A Vac. Surf. Film. 30 (2012) 10, https://doi.org/10.1116/1.3698592.

[31] W.Y. Ching, Y.N. Xu, L. Ouyang, Electronic and dielectric properties of insulating Zr3N4, Phys. Rev. B - Condens. Matter Mater. Phys. 66 (2002) 1–10, https://doi.org/10.1103/PhysRevB.66.235106.

[32] T. Dinh, H.P. Phan, A. Qamar, P. Woodfield, N.T. Nguyen, D.V. Dao, Thermoresistive effect for advanced thermal sensors: fundamentals, design considerations, and applications, J. Microelectromech. Syst. 26 (2017) 966–986, https://doi.org/10.1109/JMEMS.2017.2710354.

[33] Z. Li, Y. Liu, R. Wu, A. Chang, B. Zhang, New linear high-temperature thermistors based on the xAl2O3-(1-x)CaMnO3 ceramics, Ceram. Int. 49 (2023) 18035–18041, https://doi.org/10.1016/j.ceramint.2023.02.171.

[34] T. Li, T. Shi, Z. Tang, G. Liao, J. Duan, J. Han, Z. He, Real-time tool wear monitoring using thin-film thermocouple, J. Mater. Process. Technol. 288 (2021) 116901, https://doi.org/10.1016/j.jmatprotec.2020.116901.

[35] Y. Lian, X. Chen, T. Zhang, C. Liu, L. Lin, F. Lin, Y. Li, Y. Chen, M. Zhang, W. Zhou, Temperature measurement performance of thin-film thermocouple cutting tool in turning titanium alloy, Ceram. Int. 49 (2022) 2250–2261, https://doi.org/10.1016/j.ceramint.2022.09.193.

[36] A. Ferreira, M.A. Correa, J.P. Silva, D. Correia, S. Lanceros-Mendez, F. Vaz, Multifunctional hard coatings based on CrNx for temperature sensing applications, Sens. Actuators A Phys. 329 (2021), https://doi.org/10.1016/j.sna.2021.112794.

[37] R. Lamni, R. Sanjinés, M. Parlinska-Wojtan, A. Karimi, F. Lévy, Microstructure and nanohardness properties of Zr–Al–N and Zr–Cr–N thin films, J. Vac. Sci. Technol. A Vac. Surf. Films 23 (2005) 593–598, https://doi.org/10.1116/1.1924579.

[38] L. Rogström, L.J.S. Johnson, M.P. Johansson, M. Ahlgren, L. Hultman, M. Odén, Age hardening in arc-evaporated ZrAlN thin films, Scr. Mater. 62 (2010) 739–741, https://doi.org/10.1016/j.scriptamat.2010.01.049.

[39] L. Rogström, L.J.S. Johnson, M.P. Johansson, M. Ahlgren, L. Hultman, M. Odén, Thermal stability and mechanical properties of arc evaporated ZrN/ZrAlN multilayers, Thin Solid Films 519 (2010) 694–699, https://doi.org/10.1016/j.tsf.2010.08.119.